

FEDSM-ICNMM2010-308*

EXPERIMENTAL AND NUMERICAL INVESTIGATION OF TWO-PHASE PATTERNS IN A CROSS-JUNCTION MICROFLUIDIC CHIP

Aritra Sur

Dept. of Mechanical Engineering
University of Houston
Houston, TX 77004-4006 USA

Lixin Yang

Sch. of Mechanical Engineering
Beijing Jiaotong University
Beijing, 100044 China

Dong Liu¹

Dept. of Mechanical Engineering
University of Houston
Houston, TX 77004-4006 USA

ABSTRACT

Two-phase microfluidic systems have been found in a wide range of engineering applications. Accurate determination of the two-phase flow patterns in microchannels is crucial to selecting appropriate predictive tools for pressure drop, heat and mass transfer in the microfluidic devices. Most of the prevailing two-phase flow maps developed using visualization techniques are unable to reveal the fundamental mechanisms responsible for the formation of specific flow pattern under given flow conditions. In this work, the high-speed photographic method is employed to study the liquid-gas two-phase flow in a cross-junction microfluidic chip with a rectangular cross section of 300 μm by 100 μm . The dynamics of bubbly, slug and annular flows are investigated. Numerical models using the VOF approach are developed to simulate the two-phase mixing and flow pattern formation in the microfluidic device. The roles of the inertia, viscous shear and surface tension forces in forming various two-phase flow patterns are discussed. The experimental results and the simulation data together provide a comprehensive phenomenological description of the key parameters and processes that govern the two-phase flow pattern formation in microfluidic devices.

INTRODUCTION

Two-phase microfluidic systems have been found in a wide variety of engineering applications, such as thermal management, energy conversion, chemical synthesis and biological applications [1-5]. Liquid-gas two-phase flow in the microdevices exhibits various drastically different behaviors from its counterpart in conventional macroscopic devices [6,7]. One fundamental issue is the formation and development of

two-phase flow pattern in microchannels, which can define the functionality and performance of many microfluidic devices.

Four basic flow patterns have been grossly classified for microchannel flows, namely, bubbly, slug, intermittent and annular flows, each characterizing a distinct morphological distribution of the liquid and gas phases. Two-phase flow patterns depend on various flow parameters, including the physical properties of fluids (the viscosity and interfacial tension), the rates of flow as well as the geometrical dimensions of the flow channel. Physically, the formation of specific flow patterns is governed by the competition of different forces in the microdevice. To evaluate the relative importance of these forces, the following group of dimensionless parameters can be defined:

- (1) Reynolds number: the ratio of inertia to viscous force

$$Re = \frac{\rho j D_h}{\mu}$$

- (2) Bond number: the ratio of gravitational force to surface tension

$$Bo = \frac{\rho g D_h^2}{\sigma}$$

- (3) Capillary number: the ratio of viscous force to surface tension

$$Ca = \frac{\mu j}{\sigma}$$

- (4) Weber number: the ratio of inertia to surface tension

$$We = \frac{\rho j^2 D_h}{\sigma}$$

In most cases of liquid-gas two-phase flow in microchannels, since $Bo \ll 1$, the gravitational force can be neglected. Thus, the surface tension force, the gas inertia and the viscous shear force exerted by the liquid phase are found to be the most critical forces in the formation of two-phase flow

¹ Corresponding author (Email: dongliu@uh.edu)

patterns. Their interplay can be comprehensively represented by the Reynolds number and the capillary number based on the liquid superficial velocity ($Re_L = \frac{\rho_L j_L D_h}{\mu_L}$ and $Ca_L = \frac{\mu_L j_L}{\sigma}$) and

the Weber number based on the gas superficial velocity ($We_G = \frac{\rho_G j_G^2 D_h}{\sigma}$).

In the literature, the formation and development of two-phase flow patterns in microfluidic devices have been studied extensively. Garstecki et al. [8] investigated the formation and breakup of a gas stream into bubbles in a flow focusing device (FFD). They attributed the bubble formation at low Ca to the pressure build-up in the liquid region which is caused by the reduction in the liquid flow area due to viscous dissipation. It was found that the volume of the bubbles generated is proportional to the product of the gas flow rate and the time during which the gas thread in the flow remains connected to the supply. In a later work, Garstecki et al. [9] found that the length of the gas bubbles produced in a T-junction is proportional to the flow rate ratio of the continuous phase (the liquid) to the dispersed phase (the gas). Xu et al. [10] studied the generation of monodisperse microbubbles in a T-junction microfluidic device using cross-flow shear rupturing technique. They used an air-water system and added surfactants to study the effect of surface tension on the bubble geometry. No significant impact of surface tension variation was observed on the size of the bubble generated. They concluded that the bubble size can be scaled with the velocity and viscosity of the continuous phase. Cubaud et al. [11] conducted experiments on bubble formation in a flow focusing microfluidic device. The slug length was found to be proportional to the homogenous fraction of the liquid phase. They used the level set method to numerically simulate the bubble break-up process and identified the break-up was caused by the pressure difference in the two phases. Yu et al. [12] employed the Lattice Boltzmann method (LBM) to study the bubble/slug formation mechanisms in a cross- and a converging-mixer under different flow conditions. They confirmed that the bubble breakup for at Ca is induced by the pressure difference in the liquid and gas phases. Qian and Lawal [13] used the volume of fluid (VOF) model to study the Taylor flow in a T-junction microchannel. They found the physical properties of the fluids (density, viscosity and surface tension) have negligible effects on the length of the gas slug, which, instead, increases with the gas superficial velocity and decreases with the liquid superficial velocity. Using the same VOF approach, Weber and Shandas [14] presented a numerical study of bubble formation through an orifice. They validated that the bubble formation process is controlled by the pressure difference in the liquid and gas phases.

Successful application of two-phase microfluidic technology depends crucially on the ability to predict and control the two-phase flow behaviors in microfluidic devices. The literature survey reveals that current understanding of the

fundamental mechanisms underlying the formation and development of two-phase flow patterns at the microscale is far from complete. In this work, the high-speed photographic method is employed to study the liquid-gas two-phase flow in a cross-junction microfluidic chip with a rectangular cross section of 300 μm by 100 μm . The dynamics of bubbly, slug and annular flows are measured. Numerical models using the VOF approach are developed to simulate the two-phase mixing and flow pattern development in the cross-junction device. The roles of the inertia, viscous shear and surface tension forces in various flow patterns are discussed. The experimental results and the simulation data together provide a comprehensive phenomenological description of the key parameters and processes that govern the two-phase flow pattern formation and development in microfluidic devices.

NOMENCLATURE

Bo	Bond number
Ca	capillary number
D	channel diameter, m
h	channel height, μm
j	superficial velocity, m/s
L	length of gas slug, m
p	pressure, Pa
Q	volumetric flow rate, m^3/s
Re	Reynolds number
t	time, s
u	velocity, m/s
w	channel width, μm
We	Weber number

Greek symbols

α	volume fraction
μ	viscosity, $\text{N s}/\text{m}^2$
ρ	mass density, kg/m^3
σ	surface tension, N/m
δ	liquid film thickness, m

Subscripts

L	liquid phase
G	gas phase

EXPERIMENTS

Figure 1 illustrates the experimental test loop employed to study the air-water two-phase flow in a microfluidic chip. Deionized (DI) water was delivered using a syringe pump (Harvard Apparatus 200) which can accurately set the liquid flow rate. A 2- μm microfilter (Swagelok) was used to remove the residual particles in the water flow before it enters the microfluidic chip. Air was supplied from a compressed gas cylinder and controlled with a two-stage regulator together with a series of control valves. Two mass flowmeters were arranged in parallel to measure the gas flow rates in different ranges (Omega FMA1615A is used for measuring low flow

rates and McMillan 50S-4 for high flow rates). The experimental data were read into a data acquisition system (Agilent 34970A) for processing.

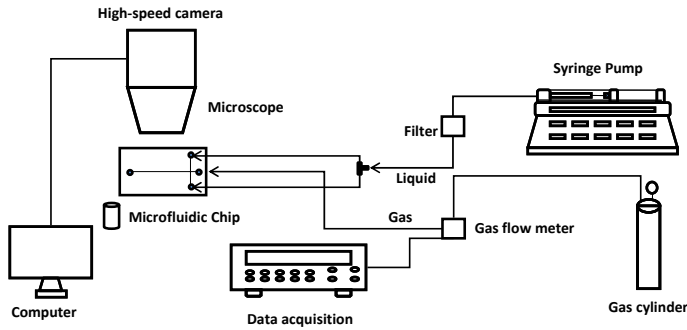


Figure 1. Two-phase flow test loop.

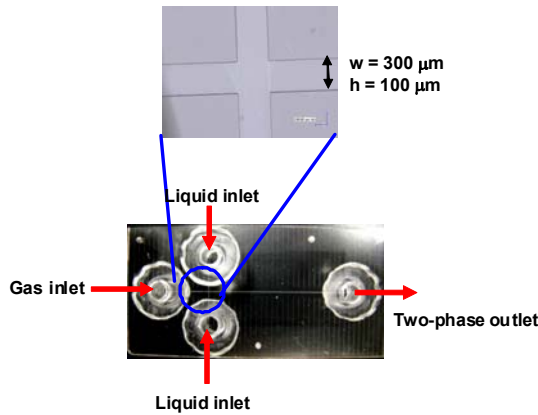


Fig. 2 Microfluidic chip.

The two-phase flow patterns were investigated on a microfluidic chip (Translume Inc.) made of fused silica glass. As shown in Fig. 2, the microfluidic chip consists of a cross-junction mixer, three inlet channels and one outlet channel. The flow channels have rectangular cross-sections with $300\ \mu\text{m}$ in width and $100\ \mu\text{m}$ in height (hydraulic diameter = $150\ \mu\text{m}$). The inlet channels are $7\ \text{mm}$ long, and the outlet channel downstream of the cross-junction is $28\ \text{mm}$ long. Water was introduced into the microfluidic chip from two side inlet ports and air from the central inlet port. The two-phase mixture was discharged at the end of the outlet channel into a collector at atmospheric pressure. All experiments were conducted at room temperature. The important physical properties of water and air are listed in Table 1.

The two-phase flow patterns were visualized using a high-speed camera (Photron APX), which can operate at a frame rate up to 120,000 frames per second (fps). In this work, the two-phase flow patterns were studied using 8,000 fps and a shutter speed of $1/120,000\ \text{s}$. The corresponding resolution of the image captured is 1024 (H) by 256 (V) pixels. A microscope (Olympus BXM) with a number of objective lenses was employed to achieve high magnification and a dynamic range of working distance. A high-power illumination source (Wite

Lite) was used to compensate for the short exposure time necessitated by the high shutter speed. In each experiment, DI water, stored in a 10-ml airtight syringe, was dispensed at a constant flow rate Q_L using the syringe pump. The gas flow rate Q_G was adjusted carefully with the control valves. The two-phase flow pattern was monitored in real time using the high-speed camera at the cross-junction as well as at several downstream locations of the microfluidic chip. A steady state was deemed to achieve when no changes in the flow pattern can be visually observed. Each steady-state value of flow rate measurements was calculated as an average of over 200 readings. The two-phase flow patterns were recorded for a period of 2 seconds. Then the fluid flow rates were adjusted with small increment for the next test, and the procedure repeated for subsequent tests.

Table 1. Physical properties of water and air.

Material	Density $\rho\ (\text{kg/m}^3)$	Viscosity $\mu\ (\text{N}\cdot\text{s/m}^2)$	Surface tension $\sigma\ (\text{N/m})$
Water	997	855×10^{-6}	0.072
Air	1.16	184.6×10^{-7}	–

NUMERICAL SIMULATION

Model Geometry

To investigate the details of the two-phase mixing and flow pattern development in the microfluidic chip, a numerical model was developed using a computational fluid dynamics (CFD) software package, CFD-ACE+ (ESI).

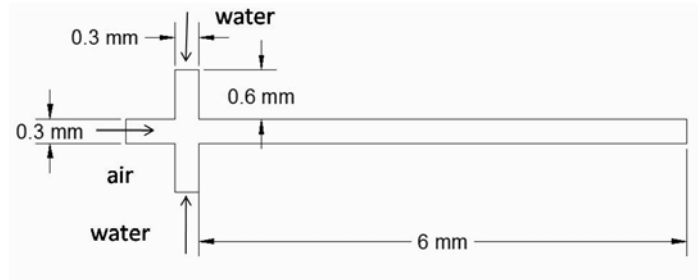


Fig. 2 CFD Model of the microfluidic chip in the numerical simulation.

Figure 2 shows the computational domain of the microfluidic chip where the liquid phase (water) is fed from the two side channels and the gas phase (air) enters the cross-junction from the main channel. In the simulation, the computational mesh is locally refined in the mixer region and near the wall in the flow channels to improve resolution of the flow details. The no-slip boundary conditions are applied to the walls. The flow velocities are specified at the liquid and gas inlets, respectively. The atmospheric pressure is imposed at the outlet. In this model, the length of the outlet channel downstream of the mixer is shortened to $6\ \text{mm}$ (20 times the channel width), instead of its full length, for the sake of

computational efficiency, because it was found to bear insignificant impact on the two-phase flow pattern formation process in the mixer.

Methodology

The volume of fluid (VOF) method was adopted to track the interface between the gas and liquid phases in the two-phase flow simulation. In this approach, the gas-liquid interface movement is described by the distribution of the volume fraction of the gas phase in the computational cells, α_G . For instance, the cell is full of liquid if $\alpha_G = 0$, the cell is full of gas if $\alpha_G = 1$, or an interface exists if $0 < \alpha_G < 1$. In general, the isocontour of $\alpha_G = 0.5$ can be used to identify the interfacial location for computation and visualization purposes. The upwind scheme with the piecewise linear interface construction (PLIC) method was applied to reconstruct the free interface [15]. The surface forces were treated using the continuum surface force (CSF) model [16]. A contact angle of 38° was specified at the liquid-wall contact.

A single set of mass and momentum equations were solved throughout the computational domain to obtain the velocity field shared by both the gas and liquid phases.

$$\frac{\partial \rho}{\partial t} + \nabla \cdot (\rho \bar{u}) = 0 \quad (1)$$

$$\frac{\partial (\rho \bar{u})}{\partial t} + \nabla \cdot (\rho \bar{u} \bar{u}) = -\nabla p + \nabla \left[\mu (\nabla \bar{u} + \nabla \bar{u}^T) \right] + \rho \bar{g} + \bar{F} \quad (2)$$

where ρ and μ are the volume-fraction-averaged properties, given as

$$\rho = \alpha_L \rho_L + \alpha_G \rho_G \quad (3)$$

$$\mu = \alpha_L \mu_L + \alpha_G \mu_G \quad (4)$$

The volume fraction of the gas phase was computed by solving the scalar convection equation

$$\frac{\partial \alpha_G}{\partial t} + \bar{u} \cdot \nabla \alpha_G = 0 \quad (5)$$

The liquid volume fraction can be then obtained

$$\alpha_L + \alpha_G = 1 \quad (6)$$

In the simulation, the fluids were considered incompressible and the flow inside the channel is laminar.

The mass and momentum conservation equations were discretized with the control volume approach. The explicit integration scheme was used for the continuity equation. The second-order central difference scheme was adopted with the adaptive damping for the momentum equation. The semi-implicit method for pressure-linked equations consistent (SIMPLEC) scheme was used for the pressure-velocity coupling, and the conjugate gradient squared (CGS) method and the algebraic multigrid (AMG) technique were employed to solve the resulting non-symmetrical and symmetric systems. In exploring the transient gas-liquid two-phase flow behaviors, the Crank-Nicolson scheme was used to provide the second-order accuracy in time. To improve computational stability and accuracy, auto time-step was activated and the Courant-

Friedrichs-Lewy (CFL) number was set to 0.03 to control the maximum stable time-step size.

RESULTS AND DISCUSSION

Two-Phase Flow Patterns

The adiabatic two-phase flow experiments were conducted for various combinations of liquid and gas flow rates. Three typical two-phase flow patterns, bubbly, slug and annular flows, were observed in the main channel (i.e., the channel downstream of the mixer), as shown in Figs. 3 (a) to (c). The bubbly flow is characterized by the occurrence of isolated, monodispersed spherical bubbles. The slug flow comprises of elongated gas bubbles which are alternatively segmented by thick liquid slugs. The gas bubbles usually take the form of a Taylor bubble with a bullet-like nose and a relatively flatter tail. Annular flow is characterized by a continuous gas core through the center of the flow channel surrounded by a liquid layer. The thickness of the liquid layer decreases with increasing gas flow rate.

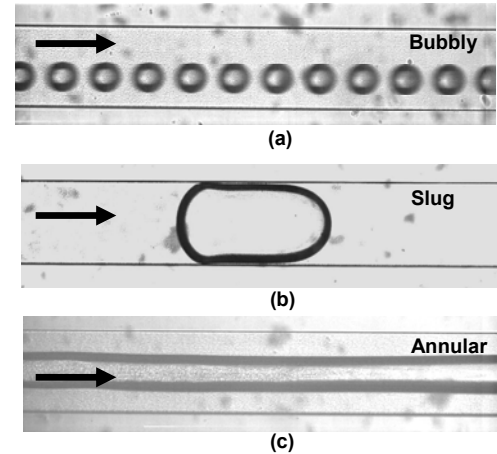


Fig. 3 Two-phase flow patterns in a microchannel.

Numerical simulations using CFD-ACE+ were also performed for selected flow conditions in the experiments as summarized in Table 2. All three typical flow patterns were considered. Figure 4 shows the comparison of the simulation results with the visualization results for the bubbly, slug and annular flows, respectively. The flow pattern formation in the cross-junction mixer as well as the fully developed flow structure at downstream location is presented. In general, the numerical model is able to capture the representative morphological features of the two-phase flow and the dynamic processes associated with the deformation and break-off of the liquid-gas interface. It is noted that in the simulated slug flow, the liquid film between the gas bubble/gas core and the channel wall is indistinguishable. This is partly attributed to the limited resolution of the present simulation.

Table 2. Flow conditions in the experiment and numerical simulation.

	j_G (m/s)	j_L (m/s)	Ca_L	Re_L	We_G	Flow Pattern
1	0.12	1.54	0.024	242	22.8	Bubbly
2	0.20	0.29	0.0038	45	0.7	Slug
3	4.74	0.07	0.0009	11	99.5	Annular

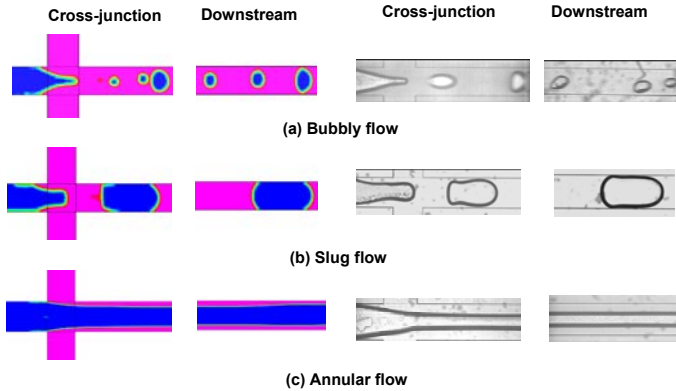


Fig. 4 Simulation vs. experimental results for three typical flow patterns. (a) Bubbly, (b) slug and (c) annular flow.

Flow Pattern Development

To study the physical mechanisms governing the development of specific flow patterns, the mechanistic effects of flow parameters can be examined in terms of the dimensionless numbers, Ca_L , Re_L and We_G , as provided in Table 2. In the following section, the formation of the bubbly, slug and annular flow patterns will be discussed, respectively, with resort to the numerical simulation results, since they can provide detailed information of the void fraction, local velocity and pressure fields, which is not easily attainable from the experimental measurements. Nonetheless, the visualization results will be presented whenever available for validation purpose.

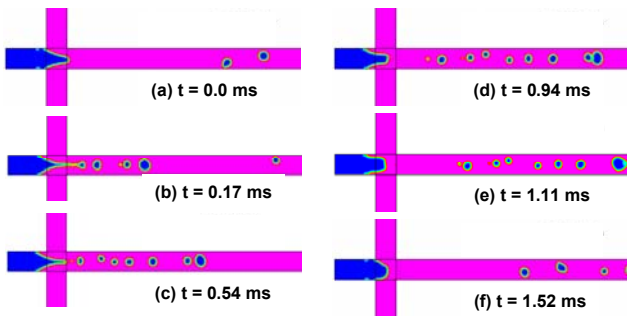


Fig. 5 Bubbly flow development as a function of time ($J_G = 0.12$ m/s, $J_L = 1.54$ m/s).

Bubbly flow

Figure 5 depicts the formation of the bubbly flow pattern at $Ca_L = 0.024$, $Re_L = 242$ and $We_G = 22.8$. Recall the physical meaning of the dimensionless numbers, it can be concluded that

the surface tension force is insignificant as compared to the viscous shear force and the inertia force, since $Ca_L > 0.01$ and $We_G \gg 1$. Therefore the break-up of the gas stream and the bubble formation are determined by the gas inertia and the viscous force shear exerted by the liquid on the interface. The physical process in Fig. 5 can be described as follows: (1) the gas stream penetrates into the main channel due to its inertia, and the surface tension is not strong enough to hold the spherical shape of the interface; (2) the shear force squeezes the gas phase into a thin stream in the cross-junction; and (3) bubbles eventually break off from the tip of the gas stream which then retracts to the end of the gas inlet channel, and the process repeats. It is noted that the bubbly flow occurs at a high liquid superficial velocity; the resulting bubble shedding frequency is around 8,000 Hz, making it difficult to clearly identify the liquid-gas interface even with a high-speed camera at 8,000 fps, which can be manifested by the blurred bubble image in Fig. 4 (a).

Slug flow

Figure 6 shows the slug formation at $Ca_L = 0.0038$, $Re_L = 45$ and $We_G = 0.7$. Under these flow conditions, the surface tension force dominates over the gas inertia and the shear stresses on the interface, and the dynamics of bubble break-up is determined by the pressure drop across the gas slug as it forms [9,12]. The slug formation starts with the front of the gas stream entering the main channel and partially blocking the cross section. The reduced flow area leads to an increased resistance to the continuous flow of the liquid phase, which causes a pressure build-up in the liquid stream. The liquid pressure force continues to squeeze the gas-liquid interface. When it is high enough to overcome the surface tension force that holds the interface together, the neck connecting the bubble and the gas stream will be cut off and the slug forms. The length of the gas slug in a T-junction microfluidic chip was found to be solely determined by the ratio of the volume flow rates of the liquid and gas phases [8]. The same argument can be extended to the current cross-junction geometry using a simple scaling analysis as follows.

From Fig. 6, the thickness of the neck decreases at a rate approximately equal to twice the superficial velocity of the liquid

$$u_{squeeze} \approx 2j_L \quad (7)$$

Thus the time needed for the break-up of the neck is

$$t \approx d / u_{squeeze} \approx w / (2j_L) \quad (8)$$

where d is the initial thickness of the neck. During this time period, the tip of the gas stream grows at a rate of j_G . So the final length of the gas slug L is

$$L \approx w + (d / u_{squeeze}) j_G \approx w(1 + 0.5 j_G / j_L) \quad (9)$$

Using the simulation condition ($j_G/j_L = 2/3$), Eq. (9) predicts $L/w \approx 1.33$, which is in reasonable agreement with the numerical measurement of $L/w \approx 1.47$ obtained from Fig. 6.

Other morphological parameters to provide a complete description of the slug flow include the length of the liquid slug, the thickness of the liquid film between the gas bubble and the wall as well as the slug generation frequency. These important parameters are not amenable to the scaling analysis, and further investigation is needed to develop predictive tools that can be used in microfluidic applications.

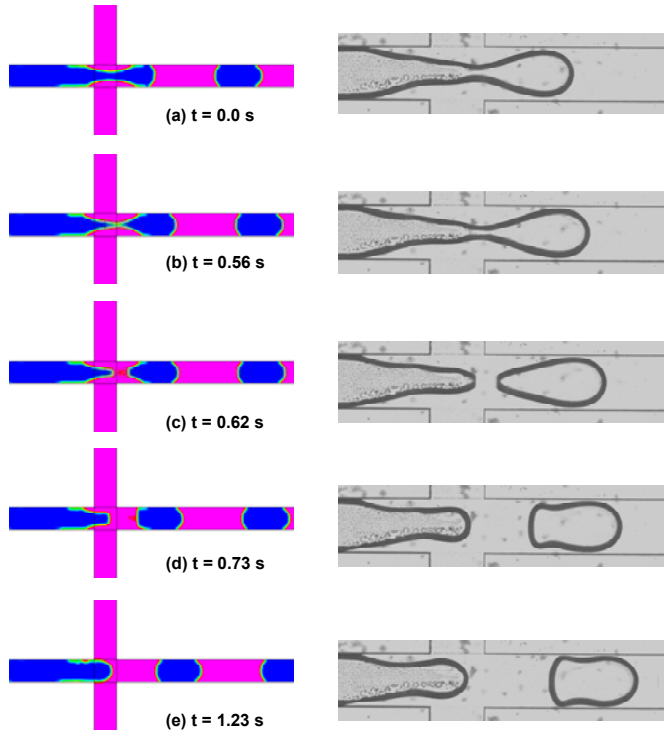


Fig. 6 Slug flow development as a function of time ($J_G = 0.20$ m/s, $J_L = 0.29$ m/s).

Annular flow

Annular flow occurs at very low Ca_L number ($Ca_L = 0.0009$) and high We_G number ($We_G = 99.5$), suggesting that the viscous shear force only plays a minor role in annular flow development as compared to those of surface tension and gas inertia. As shown in Fig. 4 (c), the annular flow is a quasi-steady flow pattern, unlike the bubbly and slug flow both having a dynamic evolution. Hence, no additional simulation and experimental results are presented here. In the annular flow, the high gas inertia sustains a continuous gas core in the main channel. The surface tension helps to mitigate and/or eliminate any interfacial deformation that arises from the shear stress-induced instabilities (because the interfacial free energy will increase unfavorably as the interfacial deformation generates new liquid-gas interface). However, at very high gas flow rates, it is expected that the shear stress exerted from the gas side will distort the interface and lead to more complicated interfacial structures.

Summary

From the above discussion, it is clear that the formation and development of different two-phase flow patterns are primarily controlled by the interplay of the gas inertia, the surface tension force and the liquid viscous shear. (1) The gas inertia creates the momentum for the gas stream to penetrate into the liquid phase. It counteracts the squeezing effects due to the liquid pressure, which may increase significantly when the liquid flow passage is blocked, and the surface tension. The overall effect of the gas inertia is to maintain a continuous gas stream. (2) The surface tension force acts as a stabilizing force. It resists the deformation of the liquid-gas interface by sustaining the interfacial Laplace pressure jump, and hinders the generation of new liquid-gas interface by retarding the shedding of gas bubbles and slugs from the continuous gas stream. It also helps to eliminate the interfacial waves arising from shear-induced instabilities. (3) The viscous shear stress exerted by the liquid on the liquid-gas interface tends to deform the smooth interface, contributing to the formation of discrete phases or wavy interface. However, at very gas flow rates, the viscous shear from the gas side will become dominant and cause the interface to rupture; consequently, the liquid film in the annular flow may locally dry out.

CONCLUSION

In this work, the formation and development of two-phase flow patterns in a cross-junction microfluidic chip was studied both experimentally and numerically. The dynamics of bubbly, slug and annular flows were measured using the high-speed photographic method. Numerical models using the VOF approach were developed to simulate the two-phase mixing and flow pattern development in the cross-junction device. The roles of the inertia, viscous shear and surface tension forces in various flow patterns were discussed. The experimental results and the simulation data together provide a comprehensive phenomenological description of the key parameters and processes that govern the two-phase flow pattern formation and development in microfluidic devices

REFERENCE

- ¹ Garimella, S. V., Singhal, V., and Liu, D., On-chip thermal management with microchannel heat sinks and integrated micropumps, Proc. IEEE 94:1534-1548, 2006..
- ² Yen, T. J., Zhang, X., Lu, G. Q., and Wang, C. Y., A micro methanol fuel cell operating at near room temperature, Appl. Phys. Lett. 83:4056-4058, 2003.
- ³ Gavriilidis, A., Angeli, P., Cao, E., Yeong, K. K., and Wan, Y. S. S., Technology and applications of microengineered reactors, Chem. Eng. Res. Des. 80:3-30, 2002.
- ⁴ Auroux, P. A., Iossifidis, D., Reyes, D. R., and Manz, A., Micro total analysis systems. 2. Analytical standard operations and applications, Anal. Chem. 74:2637-2652, 2002..
- ⁵ Thorsen, T., Maerkl, S. J., and Quake, S. R., Microfluidic large-scale integration, Science 298:580-584, 2002.

- ⁶ Bergles, A. E., Lienhard, V. J. H., Kendall, G. E., and Griffith, P., Boiling and evaporation in small diameter channels, *Heat Transfer Eng.* 24:18-40, 2003.
- ⁷ Thome, J. R., Boiling in microchannels: A review of experiment and theory, *Int. J. Heat Fluid Flow* 25:128-139, 2004.
- ⁸ Garstecki, P., Stone, H. A., and Whitesides, G. M., Mechanism for flow-rate controlled breakup in confined geometries: A route to monodisperse emulsions, *Phys. Rev. Lett.* 94: 164501, 2005.
- ⁹ Garstecki, P., Fuerstman, M. J., Stone, H. A., and Whitesides, G. M., Formation of droplets and bubbles in a microfluidic T-junction - scaling and mechanism of break-up, *Lab Chip* 6: 437-446, 2006.
- ¹⁰ Xu, J. H., Li, S. W., Wang, Y. J., and Luo, G. S., Controllable gas-liquid phase flow patterns and monodisperse microbubbles in a microfluidic T-junction device, *Appl. Phys. Lett.* 88: 133506, 2006.
- ¹¹ Cubaud, T., Tatineni, M., Zhong, X., and Ho, C.-M., Bubble dispenser in microfluidic devices, *Phys. Rev. E* 27: 037302, 2005.
- ¹² Yu, Z., Hemminger, O., and Fan, L. S., Experiment and lattice Boltzmann simulation of two-phase gas-liquid flows in microchannels, *Chem. Eng. Sci.* 62: 7172-7183, 2007.
- ¹³ Qian, D., and Lawal, A., Numerical study on gas and liquid slugs for Taylor flow in a T-junction microchannel, *Chem. Eng. Sci.* 61: 7609-7625, 2006.
- ¹⁴ Weber, M. W., and Shandas, R., Computational fluid dynamics analysis of microbubble formation in microfluidic flow-focusing devices, *Microfluid. Nanofluid.* 3: 195-206, 2007.
- ¹⁵ Youngs, D. L., Time-dependent multi-material flow with large fluid distortion, in: Morton, K. W., Baibnes, M. J., (Eds.), *Numerical Methods for Fluid Dynamics*, Academic Press, NY, 1982.
- ¹⁶ Brackbill, J. U., Kothe, D. B., Zemach, C., A continuum method for modeling surface tension, *J. Compt. Phys.* 100: 3350354, 1992.